

Indirect evidence of significant grain growth in young protostellar envelopes from polarized dust emission

Valeska Valdivia,^{1*} Anaëlle Maury,¹ Robert Brauer,¹ Patrick Hennebelle,¹
Maud Galametz,¹ Vincent Guillet,^{2,3} and Stefan Reissl⁴

¹Laboratoire AIM, Paris-Saclay, CEA/IRFU/SAP - CNRS - Université Paris Diderot, 91191 Gif-sur-Yvette Cedex, France

²Institut d'Astrophysique Spatiale, CNRS, Univ. Paris-Sud, Univ. Paris-Saclay, Bât. 121, 91405 Orsay Cedex, France

³LUMP, Université de Montpellier, CNRS/IN2P3, CC 72, Place Eugène Bataillon, 34095 Montpellier Cedex 5, France

⁴Universität Heidelberg, Zentrum für Astronomie, ITA, Albert-Ueberle-Str. 2, 69120 Heidelberg, Germany

Accepted XXX. Received YYY; in original form ZZZ

ABSTRACT

How and when in the star formation sequence do dust grains start to grow into pebbles is a cornerstone question to both star and planet formation. We compute the polarized radiative transfer from a model solar-type protostellar core, using the POLARIS code, aligning the dust grains with the local magnetic field, following the radiative torques (RATs) theory. We test the dependency of the resulting dust polarized emission with the maximum grain size of the dust size distribution at the envelope scale, from $a_{\max} = 1 \mu\text{m}$ to $50 \mu\text{m}$. Our work shows that, in the framework of RAT alignment, large dust grains are required to produce polarized dust emission at levels similar to those currently observed in solar-type protostellar envelopes at millimeter wavelengths. Considering the current theoretical difficulties to align a large fraction of small ISM-like grains in the conditions typical of protostellar envelopes, our results suggest that grain growth (typically $> 10 \mu\text{m}$) might have already significantly progressed at scales 100–1000 au in the youngest objects, observed less than 10^5 years after the onset of collapse. Observations of dust polarized emission might open a new avenue to explore dust pristine properties and describe, for example, the initial conditions for the formation of planetesimals.

Key words: polarization – magnetic fields – methods: numerical – stars: protostars

1 INTRODUCTION

In our quest to understand both star and planet formation, one cornerstone question is how dust grains evolve from their pristine properties in the interstellar medium (ISM) to planetesimals in Class II disks, where observations suggest that grains from subnanometric sizes to cm pebbles co-exist (see, e.g. Testi et al. 2014, for a review). While understanding the transition from pebbles to planets is the focus of many circumstellar disk studies, characterizing the early stages of grain growth is at least as important, not only to put constraints on the initial dust grain size distribution for disk evolution (see, e.g. Birnstiel et al. 2016, for a review), but to address several key issues such as the formation of complex organic molecules (see, e.g. Herbst 2017, for a review) or characterize the coupling of the magnetic field with the gas in star-forming cores (e.g. Zhao et al. 2018). A remaining open question is how and when the initial fractal growth

of ISM grains to micronic aggregates proceeds, from which grains can further grow by grain-grain collisions and ram pressure of the gas (Blum & Wurm 2008; Dominik et al. 2016). Analytical and numerical models of grain growth in cores (Ormel et al. 2011; Chacón-Tanarro et al. 2017) suggested that ISM grains can grow up to $\sim 100 \mu\text{m}$ sizes over the estimated lifetime of prestellar cores (1 Myr, e.g. Könyves et al. 2015). In molecular clouds and dense cold cores, the observed decrease in the mid-IR to far-IR emission ratio (Stepnik et al. 2003; Flagey et al. 2009), the increase in the dust far-IR/millimeter opacity and spectral index (Martin et al. 2012; Bracco et al. 2017), and the increased scattering efficiency from the near- to mid-IR (Paganì et al. 2010) point out to an evolution of dust properties in dense regions. It was suggested that these observations could be explained if dense structures contain aliphatic-rich ice-mantled grains (Jones et al. 2013; Ysard et al. 2016), or already evolved micrometer-sized grains (Steinacker et al. 2010; Lefèvre et al. 2016).

A rather unexplored step on the evolutionary sequence lead-

* E-mail: valeska.valdivia@cea.fr

ing to the formation of planets is the protostellar stage, and even more so the main accretion phase (Class 0 protostars, André et al. 2000). During this short ($< 10^5$ years) but cornerstone phase for both the formation of stars and disks, half of the final stellar mass is accreted from the surrounding envelope into the stellar embryo: in about a free-fall time a typical dust grain (coupled to the gas) will drift from the outer protostellar envelope towards the much higher density, higher temperature, inner region. While the early stages of the formation and evolution of disks around protostars remain a very active research topic both observationally and theoretically (Maury et al. 2019; Wurster & Li 2018), it is yet very difficult to find robust tracers of the dust properties in these Class 0 disks and envelopes: only a few studies suggested dust spectral indices compatible with grain growth (in 3 objects, Kwon et al. 2009).

In the presence of a magnetic field, non-spherical spinning dust grains will precess around magnetic field lines (Davis & Greenstein 1951; Purcell 1979), aligning their long axis perpendicular to the local magnetic field lines, producing a polarized thermal dust emission (Roberge 2004). Among the mechanisms able to align the dust grains, the Radiative Alignment Torques (RATs, Draine & Weingartner 1997; Hoang & Lazarian 2014), has become recently the favoured alignment process in the diffuse ISM (see Andersson et al. 2015, and references therein): in the current RATs theory, the absorption and scattering of photons exert a differential torque that spins up, precesses and aligns helical dust grains. The RATs alignment torques act on short timescales ($10^3 - 10^4$ yr) and are more efficient than the magnetic relaxation (Draine & Weingartner 1997). The efficiency of the RATs mechanism depends, among other parameters, on the strength and spectral energy distribution of the incoming radiation field, and thus on the size of the dust grains (Draine & Weingartner 1996; Cho & Lazarian 2007): in this paper we study the potential of the polarized dust emission, in the RATs framework, to constrain the dust size distribution in protostellar cores.

2 POLARIZED DUST RADIATIVE TRANSFER

To test the effect of the dust size distribution we post-process a snapshot of a non-ideal magnetohydrodynamical (MHD) simulation performed with the RAMSES code (Teyssier 2002; Fromang et al. 2006). The simulation, described in more detail in Valdivia et al. (in prep), follows the magnetized collapse of a $2.5 M_{\odot}$ dense core with a mass-to-flux ratio $\mu = 6.6$ and a ratio between the rotational and gravitational energy of $E_{\text{rot}}/E_{\text{grav}} = 10^{-2}$. The full size of the simulation is 0.167 pc (~ 34481.6 au) and the effective resolution is ~ 1 au.

We selected a time step where the protostar has already accreted $0.2 M_{\odot}$, which reproduces the typical conditions of a young protostar in its main accretion phase. Figure 1 shows the total column density (N), as well as the integrated magnetic field strength (B) and orientation. Additionally, we provide the mean radial profile of the gas density in Fig. A1.

We perform the radiative transfer using the POLARIS code (Reissl et al. 2016), capable of dust heating, thermal emission, and calculating the grain alignment heating efficiency of

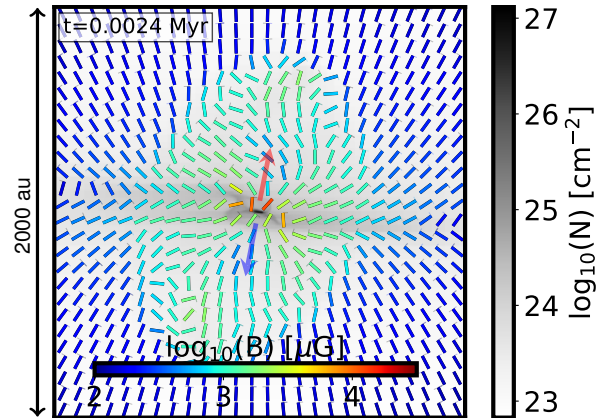


Figure 1. Column density distribution (background gray scale), from the modeled protostellar core at a scale of 2000 au (the core extends over 7000 au in our simulation). Note that the core is seen almost edge-on, with the outflow lying in the plane of the sky, creating the north-south bubbles seen here. Overlaid are the mean magnetic field lines orientation, color-coded by magnetic field intensity (both obtained from line-of-sight integration, local mass-weighted, of the magnetic field projected onto the plane of the sky). The arrows indicate the outflows direction.

non-spherical dust grains with the local magnetic field lines following the RATs theory of Lazarian & Hoang (2007) as outlined in Hoang & Lazarian (2014). We model the central source as a blackbody of $2 L_{\odot}$ (of radius $1 R_{\odot}$), similar to typical accretion luminosities observed towards low-mass young protostars (Dunham et al. 2014). We also include the interstellar radiation field (ISRF) as an external radiation field of strength $G_0 = 1$, using the Mathis et al. (1983) description. We assume a gas-to-dust mass ratio of 100, and a composition of 62.5% astronomical silicates and 37.5% graphite grains, that fits the Galactic extinction curve (Mathis et al. 1977). The dust grains are supposed oblate, with an aspect ratio of 0.5 (Hildebrand & Dragovan 1995). We use a MRN-like dust size distribution (Mathis et al. 1977), described by $dn(a) \propto a^{-3.5} da$, where a , the effective radius of the grain, is the radius of a sphere of equivalent volume, and $n(a)$ is the number of dust grains of effective radius a . To test the influence of the presence of larger grains on the polarized dust emission we set the minimum dust grain size to $a_{\text{min}} = 5$ nm, and we vary the maximum size of the distribution from $a_{\text{max}} = 1 \mu\text{m}$ to $50 \mu\text{m}$ keeping the total dust mass constant. Our simulation reproduces the standard opacities observed in embedded protostars, resulting in a radiation field dominated by low energy photons at the envelope scales. The size distribution and the choice of the dust composition used here do not greatly impact the opacity. We produce synthetic polarized dust emission maps for the central 8000 au at a slightly lower resolution than available in the native simulation (10 au per pixel), at the two wavelengths observations of the dust polarized emission that are the most regularly carried out in current observational facilities ($\lambda = 0.8$ mm, and 1.3 mm). Note that the dust thermal emission is optically thin at these two wavelengths, throughout most of the spatial scales $r > 50$ au investigated here (see Fig. A4).

POLARIS produces maps of the Stokes parameters I , Q and U , from which we build perfect (not including any

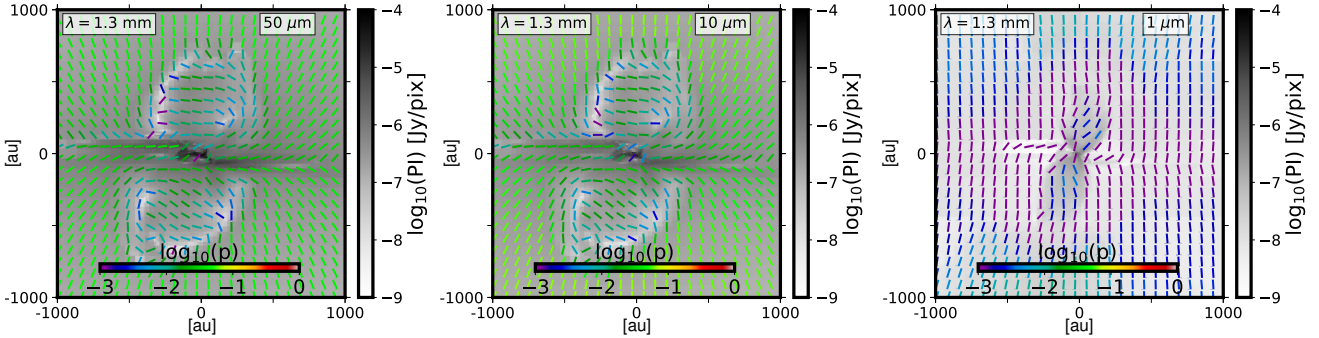


Figure 2. Perfect synthetic observations at $\lambda = 1.3$ mm showing the polarized emission (background image), and the inferred magnetic field orientation line segments, for which we have color coded the polarization fraction. a_{\max} is given on the top-right corner of each panel. The full set of dust distributions is shown in Fig. A5

instrumental effect) total linearly polarized emission maps (polarized intensity $PI = (Q^2 + U^2)^{0.5}$), and polarization fraction ($p = PI/I$) maps. In Valdivia et al. (in prep), the instrumental effects have been included and show not to affect the polarization fractions by more than 50% in regions where the total dust thermal emission (Stokes I) is detected with a signal-to-noise ratio > 5 (standard debiasing). Finally, we produce synthetic magnetic field ‘vectors’ maps by rotating by 90° the polarization angle ψ obtained as: $\psi = \frac{1}{2} \arctan(U, Q)$.

Figure 2 shows the resulting polarized dust continuum emission maps at $\lambda = 1.3$ mm, overlaid with the magnetic field orientation line segments reconstructed from the Stokes maps, for which we have color coded the recovered polarization fraction. We show the resulting maps for three dust grain size distributions, zoomed in the central 2000 au of the original map so the features in the inner envelopes can be easily distinguished. This figure shows that the resulting polarized emission strongly depends on the dust grain sizes (see the a_{align} map in Fig. A2), and especially on the maximum dust grain size of the dust distribution included in the radiative transfer. This can be easily understood since the radiative torque applied to dust grains Q depends strongly on the ratio between the incoming photon wavelength and the dust grain size (Lazarian & Hoang 2007; Hoang & Lazarian 2014). In particular, this figure shows that grains smaller than 1 or 2 μm can only be aligned in the irradiated cavities created by the bipolar outflows (bipolar feature seen in emission in the lower panel), where photons from the accreting protostar can travel more freely. With such grain size distributions, the resulting polarization fraction on the lines of sight probing the envelope remain very low ($p < 1\%$), even for a pure silicate composition (see Fig. A8). Only when including dust grains with sizes up to 10 μm , the envelope polarized emission is recovered from the high density equatorial region at polarization fractions $p > 1\%$.

In Fig. 3 we present the radial profiles of the total dust thermal emission (left panels), polarized intensity (middle panels) and polarization fraction (right panels), for the dust grain size distributions explored, at the two wavelengths $\lambda = 0.8$ mm (top row) and $\lambda = 1.3$ mm (bottom row). The dust thermal emission shows a decrease towards the outer regions of the envelope, consistent with the decrease of the column densities and dust temperature, which remains quite

insensitive to the dust size distribution (see Fig. A3). Even though the dust size distribution has a mild influence on the total dust emission, the center and right panels show that the effect on its polarized component is very strong, producing a variation of the polarization fraction of roughly two orders of magnitude in the inner envelope ($r < 1000$ au, and densities higher than 10^7 cm^{-3}). The polarized intensity increases with a_{\max} until $a_{\max} \sim 30 \mu\text{m}$. Since the total dust mass is kept constant, the cross section per unit mass decreases with a_{\max} , and as the efficiency of absorption and emission do not increase further for distributions with larger grains, the contribution to the polarized emission starts to decrease. This is more striking in the case of the polarization fraction, where the distribution with $a_{\max} \sim 50 \mu\text{m}$ shows a lower polarization fraction.

3 POLARIZED DUST EMISSION AS AN INDICATOR OF EARLY GRAIN GROWTH IN YOUNG PROTOSTARS?

It is only in the last decade that observations of the polarized dust emission in the inner regions of low-mass protostellar cores, at scales $\lesssim 1000$ au could be carried out, starting with the advent of polarization capabilities on the Submillimeter Array (SMA, Girart et al. 2006; Gonçalves et al. 2008; Frau et al. 2011; Rao et al. 2009; Galametz et al. 2018) and the Combined Array for Research in Millimeter-wave Astronomy (CARMA, Stephens et al. 2013; Hull et al. 2014; Segura-Cox et al. 2015). Since 2016 the most sensitive sub-millimeter interferometer, ALMA, is producing exquisite polarized dust continuum emission maps from the high-density protostellar interiors, probing the properties of polarized emission down to scales of a few tens of au. Typically, polarization fractions of $p \sim 2 - 10\%$ are recovered in envelopes at radii $> 50 - 5000$ au, when both self-scattering polarization and large filtering effects can be excluded (e.g., Kataoka et al. 2015; Hull et al. 2017a; Maury et al. 2018; Cox et al. 2018; Alves et al. 2018; Sadavoy et al. 2018).

All dust grain size distributions including only small grains (e.g. $< 3 \mu\text{m}$) considered in our study produce polarized emission intensities at undetectable levels with current interferometers, and polarization fractions too low by one order of magnitude with respect to observed values at similar scales in solar-type protostars (see grey region in

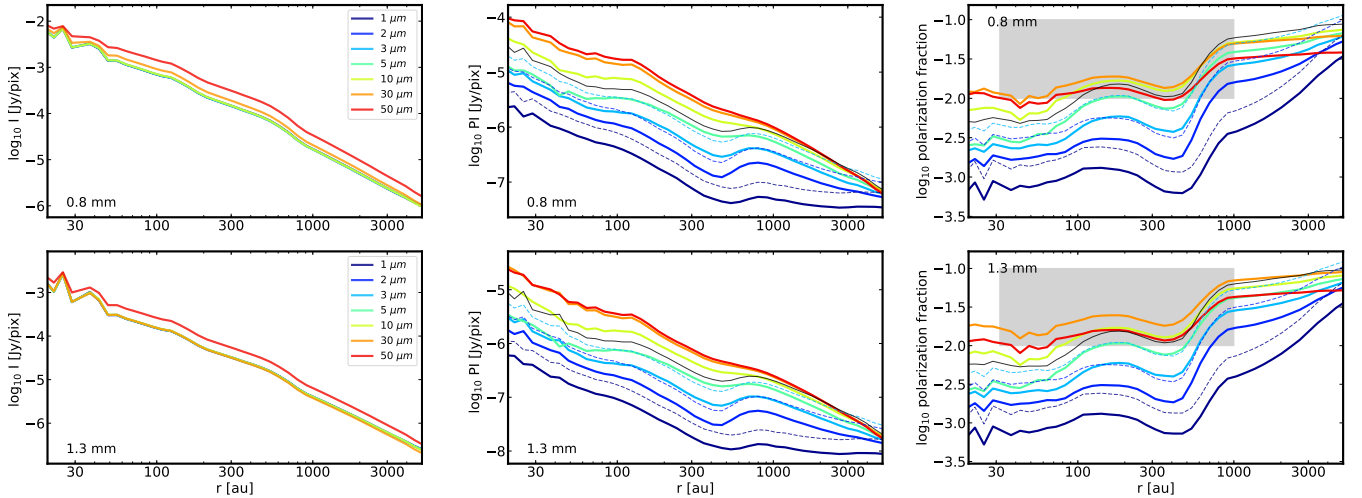


Figure 3. Radial mean profiles for two wavelengths: $\lambda = 0.8$ mm (top panels), and $\lambda = 1.3$ mm (bottom panels). From left to right: total dust emission (Stokes I), total linearly polarized intensity (PI), and polarization fraction indicating the typical values observed in YSOs (grey region). The dashed lines show the expected values assuming $f_{\text{high-}J} = 1$. The thin solid black line shows the polarization with $a_{\text{max}} = 3 \mu\text{m}$ and an unlikely size distribution of $n(a) \propto a^{-2}$ da, for reference.

Fig. 3). Indeed, the local radiation field is drastically shifted towards longer wavelengths in the high density interiors of protostellar envelopes, and since only dust grains with sizes close to the wavelength of incident photons get efficiently aligned, our models require large grains to produce polarized emission from protostellar cores at detectable levels. Furthermore, in regions with high rates of collisions, such as high pressure regions in the equatorial plane, larger grains remain aligned more easily due to their higher inertia. We stress that a harder radiation field from a higher accretion luminosity is not able to significantly increase the polarization fraction for these grain sizes (see Fig. A7). If RATs are indeed responsible for the grain alignment in dense protostellar interiors, then our results suggest that protostellar envelopes must include dust grains with typical sizes of at least $10 \mu\text{m}$ to produce polarization fractions similar to the observed values $p \gg 1\%$.

Note that, inversely, a lack of detected polarization does not suggest a lack of large grains, but can be due to various factors, such as a beam dilution or line-of-sight canceling due to turbulent or complex magnetic field topologies. Indeed, single dish observations of the dust polarized emission, probing ~ 0.1 pc scales, show a decrease in polarization fraction in denser regions $p \propto I^{-\alpha}$, with $\alpha \sim 0.5 - 1.2$ is usually found at those scales (Wolf et al. 2003; Crutcher 2004; Soam et al. 2018). High angular resolution observations suggest this is at least partly due to a beam averaging effect (unresolved structure of \mathbf{B}) since larger polarization fractions are recovered when probing typical scales 1000 au in dense cores, thanks to interferometric facilities (Hull et al. 2014, 2017b; Galametz et al. 2018). This was also suggested by early analysis of synthetic polarization maps from MHD simulations (Falceta-Gonçalves et al. 2008; Padovani et al. 2012). In the case of B335, for example, the polarization fraction decreases with the Stokes I intensity in the seven JCMT POL-2 detections (about $\sim 1\%$ on average in the inner 3000 au, see Yen et al. 2019), but is recovered at the level of $\sim 10\%$ with SMA at scales $\sim 500 - 1000$ au (Galametz et al. 2018) and

with ALMA at similar levels down to scales $\sim 50 - 100$ au (Maury et al. 2018).

Although observational studies suggest that the RATs is likely to be a dominant mechanism of grain alignment in the ISM, we acknowledge that developments regarding alignment theories are thriving and that currently the knowledge is still limited (see Lazarian 2009, for a discussion). Especially, we note that a new flavor of RATs including superparamagnetic grains (MRAT, Hoang & Lazarian 2016), able to increase the fraction of aligned grains in the high- J attractor, was developed to reproduce the high levels of polarized emission observed in the diffuse ISM by the *Planck* observatory, p up to $\sim 20\%$ (Planck Collaboration et al. 2015). Note that in case a mechanism would allow to align all dust grains, independently of their size with respect to the local radiation field (perfect alignment, see Fig. A6), then no constraints could be obtained on the dust size distribution based on the polarization fractions. However, such a mechanism is yet unconstrained: our results are valid in the current widely admitted framework of RATs dominated alignment, and should be revised if other mechanisms are shown to produce as good agreement as RATs with observations in the future. A major caveat in the RATs theory is the actual value of the fraction of dust spinning at suprathermal velocities in the high- J attractor ($f_{\text{high-}J}$), that corresponds to a highly stable population and can be considered as perfectly aligned. In our study we use a fraction $f_{\text{high-}J} = 0.25$, that fits better the polarization fractions observed in Bok globules (Brauer et al. 2016). Additionally, we give an upper limit to the polarized intensity and to the polarization fraction for the distributions with $a_{\text{max}} \leq 3 \mu\text{m}$ by assuming a rather unrealistic fraction of $f_{\text{high-}J} = 1.0$, shown in dashed lines in the same figure. Note that including the ISRF slightly enhances the alignment by the RATs mechanism only in the outer envelope layers where the ISRF photons are able to penetrate (up to 5×10^{-2} in polarization fraction for $r > 1000$ au). It has a very low impact on the polarization fraction in the inner 1000 au (typically less than 5×10^{-3} in polarization fraction). Another possible caveat is the slope of the grain size distri-

bution. We include for reference the results for PI and p for the $a_{\max} = 3 \mu\text{m}$ distribution using an unlikely slope of -2 (thin solid black line). Altogether, Fig. 3 shows that realistic dust size distributions with only small grains ($a < 3 \mu\text{m}$) can barely reach the observed degrees of polarization. Additionally, we acknowledge the difficulty to perform precise calculations for large dust grains consisting of complex aggregates (Min et al. 2009), and that the optical constants and cross sections used in grain models might not be fully accurate and need to be reassessed in the near future, at the light of the newest laboratory measurements on analogues of interstellar silicates (Demyk et al. 2017a,b). Finally, although grain growth may make grains more spherical and thus harder to align with B -fields by radiative torques, the polarization fractions observed in, e.g., the inner envelopes of Class 0 protostars cannot be explained with diffuse ISM grains only in the currently developed alignment theories.

4 CONCLUSIONS

We explore radiative transfer maps of the polarized dust continuum emission from a synthetic low-mass protostellar core. We show that, in the RATs paradigm of dust grain alignment with the magnetic field, only radiative transfer models including large grains (typically $> 10 \mu\text{m}$) are able to produce polarized dust emission at levels similar to what is currently observed at small scales within embedded protostellar cores in the (sub-)mm domain (e.g. ALMA). Our results suggest that either grains have already significantly grown at scales $100 - 1000 \text{ au}$ in the youngest protostellar envelopes observed $< 10^5$ years after the onset of collapse, or a missing alignment theory remains to be developed that would virtually align perfectly all dust grains, and this independently of their size with respect to the wavelength of the local radiation field. Considering the current theoretical difficulties to align ISM type nanometric grains at the high gas densities typical in these protostars, our work favors the possibility of grain growth and highlights the possibility to use the properties of dust polarized emission to gain access to dust pristine properties and better describe, for example, the very early stages of the formation of planetesimals.

ACKNOWLEDGEMENTS

This research has received funding from the European Research Council (ERC) under the European Union’s Horizon 2020 research and innovation programme (MagneticYSOS project, Grant Agreement No 679937).

This work was supported by the Programme National “Physique et Chimie du Milieu Interstellaire” (PCMI) of CNRS/INSU with INC/INP co-funded by CEA and CNES.

REFERENCES

- Alves F. O., et al., 2018, *A&A*, **616**, A56
 Andersson B.-G., Lazarian A., Vaillancourt J. E., 2015, *ARA&A*, **53**, 501
 André P., Ward-Thompson D., Barsony M., 2000, *Protostars and Planets IV*, p. 59
 Birnstiel T., Fang M., Johansen A., 2016, *Space Sci. Rev.*, **205**, 41
 Blum J., Wurm G., 2008, *ARA&A*, **46**, 21
 Bracco A., et al., 2017, *A&A*, **604**, A52
 Brauer R., Wolf S., Reissl S., 2016, *A&A*, **588**, A129
 Chacón-Tanarro A., Caselli P., Bizzocchi L., Pineda J. E., Harju J., Spaans M., Désert F. X., 2017, *A&A*, **606**, A142
 Cho J., Lazarian A., 2007, *ApJ*, **669**, 1085
 Cox E. G., Harris R. J., Looney L. W., Li Z.-Y., Yang H., Tobin J. J., Stephens I., 2018, *ApJ*, **855**, 92
 Crutcher R. M., 2004, *Ap&SS*, **292**, 225
 Davis Jr. L., Greenstein J. L., 1951, *ApJ*, **114**, 206
 Demyk K., et al., 2017a, *A&A*, **600**, A123
 Demyk K., et al., 2017b, *A&A*, **606**, A50
 Dominik C., Paszun D., Borel H., 2016, arXiv e-prints,
 Draine B. T., Weingartner J. C., 1996, *ApJ*, **470**, 551
 Draine B. T., Weingartner J. C., 1997, *ApJ*, **480**, 633
 Dunham M. M., et al., 2014, *Protostars and Planets VI*, p. 195
 Falceta-Gonçalves D., Lazarian A., Kowal G., 2008, *ApJ*, **679**, 537
 Flagey N., et al., 2009, *ApJ*, **701**, 1450
 Frau P., Galli D., Girart J. M., 2011, *A&A*, **535**, A44
 Fromang S., Hennebelle P., Teyssier R., 2006, *A&A*, **457**, 371
 Galametz M., et al., 2018, *A&A*, **616**, A139
 Girart J. M., Rao R., Marrone D. P., 2006, *Science*, **313**, 812
 Gonçalves J., Galli D., Girart J. M., 2008, *A&A*, **490**, L39
 Herbst E., 2017, *International Reviews in Physical Chemistry*, **36**, 287
 Hildebrand R. H., Dragovan M., 1995, *ApJ*, **450**, 663
 Hoang T., Lazarian A., 2014, *MNRAS*, **438**, 680
 Hoang T., Lazarian A., 2016, *ApJ*, **831**, 159
 Hull C. L. H., et al., 2014, *ApJS*, **213**, 13
 Hull C. L. H., et al., 2017a, *ApJ*, **847**, 92
 Hull C. L. H., et al., 2017b, *ApJ*, **847**, 92
 Jones A. P., Fanciullo L., Köhler M., Verstraete L., Guillet V., Bocchio M., Ysard N., 2013, *A&A*, **558**, A62
 Kataoka A., et al., 2015, *ApJ*, **809**, 78
 Könyves V., et al., 2015, *A&A*, **584**, A91
 Kwon W., Looney L. W., Mundy L. G., Chiang H.-F., Kemball A. J., 2009, *ApJ*, **696**, 841
 Lazarian A., 2009, in Henning T., Grün E., Steinacker J., eds, *ASP Conf. Series Vol. 414, Cosmic Dust - Near and Far*. p. 482 ([arXiv:0903.1100](https://arxiv.org/abs/0903.1100))
 Lazarian A., Hoang T., 2007, *MNRAS*, **378**, 910
 Lefèvre C., Pagani L., Min M., Poteet C., Whittet D., 2016, *A&A*, **585**, L4
 Martin P. G., et al., 2012, *ApJ*, **751**, 28
 Mathis J. S., Rumpl W., Nordsieck K. H., 1977, *ApJ*, **217**, 425
 Mathis J. S., Mezger P. G., Panagia N., 1983, *A&A*, **128**, 212
 Maury A. J., et al., 2018, *MNRAS*, **477**, 2760
 Maury A. J., et al., 2019, *A&A*, **621**, A76
 Min M., Dullemond C. P., Dominik C., de Koter A., Hovenier J. W., 2009, *A&A*, **497**, 155
 Ormel C. W., Min M., Tielens A. G. G. M., Dominik C., Paszun D., 2011, *A&A*, **532**, A43
 Padovani M., et al., 2012, *A&A*, **543**, A16
 Pagani L., Steinacker J., Bacmann A., Stutz A., Henning T., 2010, *Science*, **329**, 1622
 Planck Collaboration et al., 2015, *A&A*, **576**, A106
 Purcell E. M., 1979, *ApJ*, **231**, 404
 Rao R., Girart J. M., Marrone D. P., Lai S.-P., Schnee S., 2009, *ApJ*, **707**, 921
 Reissl S., Wolf S., Brauer R., 2016, *A&A*, **593**, A87
 Roberge W. G., 2004, in Witt A. N., Clayton G. C., Draine B. T., eds, *ASP Conf. Series Vol. 309, Astrophysics of Dust*. p. 467
 Sadavoy S. I., et al., 2018, *ApJ*, **859**, 165
 Segura-Cox D. M., Looney L. W., Stephens I. W., Fernández-López M., Kwon W., Tobin J. J., Li Z.-Y., Crutcher R., 2015, *ApJ*, **798**, L2

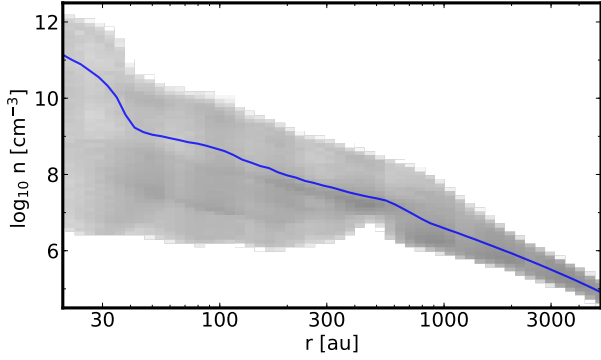


Figure A1. Local total gas number density radial distribution from the non-ideal MHD simulation. The radial number density profile shows the mean value (blue line) and the dispersion (gray) for the selected output.

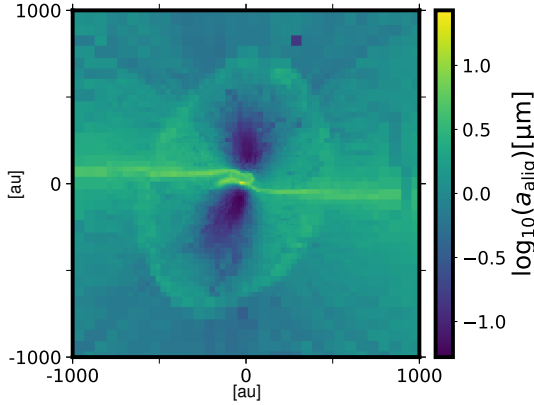


Figure A2. Mean a_{alig} in the central 50 au region for the $a_{\text{max}} = 30 \mu\text{m}$ distribution. a_{alig} is a local value and it corresponds to the minimum size at which dust grains start to align according to the local conditions in the RATs theory. In the cavities created by the outflow grains as small as $0.1 \mu\text{m}$ can start to align, while in the equatorial region, only grains larger than $10 \mu\text{m}$ can be aligned. The value shown in this figure corresponds to the mean computed in a slab (perpendicular to the line-of-sight) of thickness 50 au around the center of the simulation box.

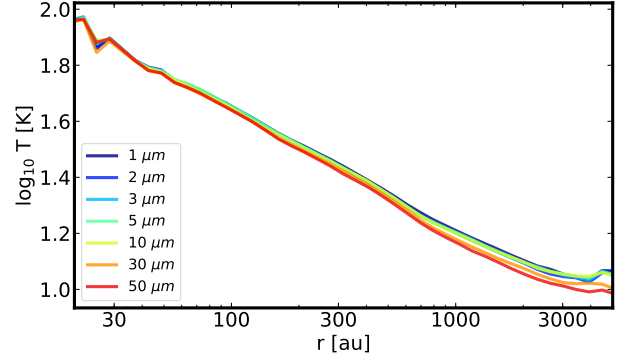


Figure A3. Radial mean dust temperature profiles for different dust distributions. a_{max} is given in the figure. The dust temperature do not strongly depend on the dust size distribution.

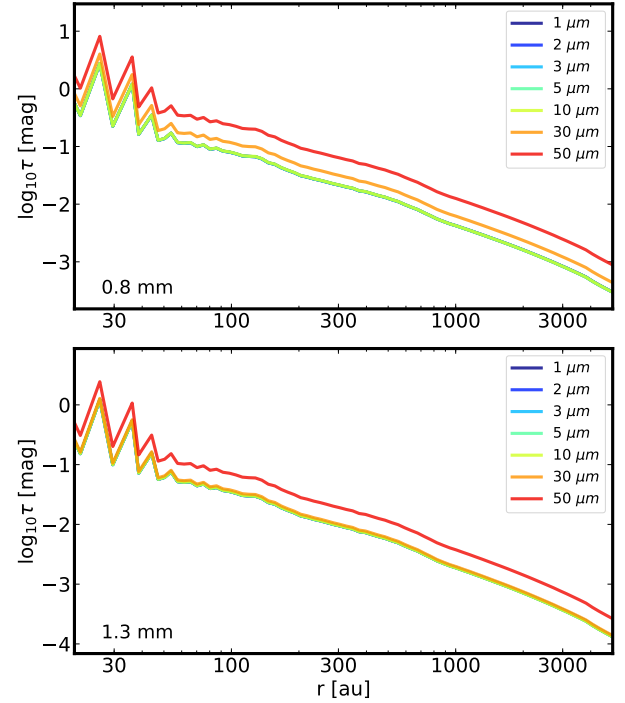


Figure A4. Radial mean opacity profiles at two wavelengths: $\lambda = 0.8$ (top), and 1.3 mm for all the dust distributions used in this paper. a_{max} is given in the figure.

APPENDIX A: SOME EXTRA MATERIAL

- Soam A., et al., 2018, *ApJ*, **861**, 65
 Steinacker J., Pagani L., Bacmann A., Guieu S., 2010, *A&A*, **511**, A9
 Stephens I. W., et al., 2013, *ApJ*, **769**, L15
 Stepnik B., et al., 2003, *A&A*, **398**, 551
 Testi L., et al., 2014, *Protostars and Planets VI*, p. 339
 Teyssier R., 2002, *A&A*, **385**, 337
 Wolf S., Launhardt R., Henning T., 2003, *ApJ*, **592**, 233
 Wurster J., Li Z.-Y., 2018, *Frontiers in Astronomy and Space Sciences*, **5**, 39
 Yen H.-W., et al., 2019, *ApJ*, **871**, 243
 Ysard N., Köhler M., Jones A., Dartois E., Godard M., Gavilan L., 2016, *A&A*, **588**, A44
 Zhao B., Caselli P., Li Z.-Y., 2018, *MNRAS*, **478**, 2723

This paper has been typeset from a $\text{\TeX}/\text{\LaTeX}$ file prepared by the author.

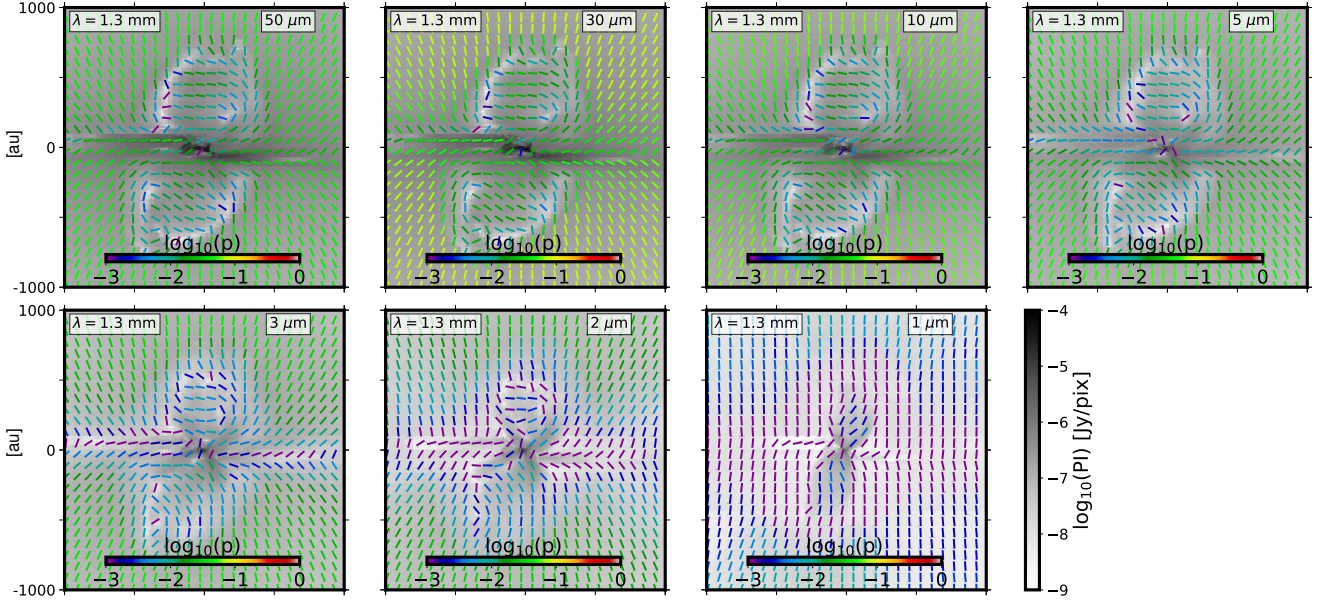


Figure A5. Full set of perfect synthetic observations at $\lambda = 1.3$ mm. The polarized dust emission (PI) is shown in gray-scale as a background image, while the inferred magnetic field orientation and polarization fraction (p) are shown as overlaid color coded segments. a_{\max} is indicated at the top-right corner of each panel.

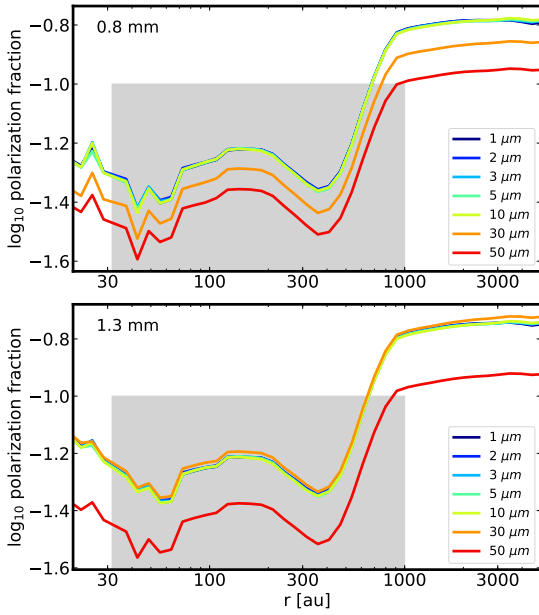


Figure A6. Radial mean polarization fraction assuming that all dust grains able to align (silicates) are perfectly aligned with the magnetic field. Results are shown for two wavelengths: $\lambda = 0.8$ mm (top panel), and $\lambda = 1.3$ mm (bottom panel). The maximum dust size for each distribution is given in the figure. The typical values observed in YSOs are shown as a grey region.

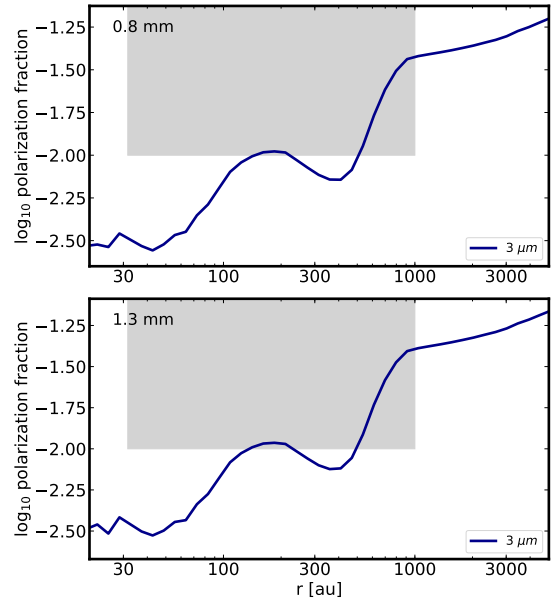


Figure A7. Radial mean polarization fraction for the distribution with $a_{\max} = 3 \mu\text{m}$, at two wavelengths: $\lambda = 0.8$ mm (top panel), and $\lambda = 1.3$ mm (bottom panel). In this case the central source is modeled as a blackbody of $10 L_{\odot}$ of radius $1 R_{\odot}$. The typical values observed in YSOs are shown as a grey region. This figure shows that even a stronger source with a harder radiation field is not able to significantly increase the amount of polarized dust emission.

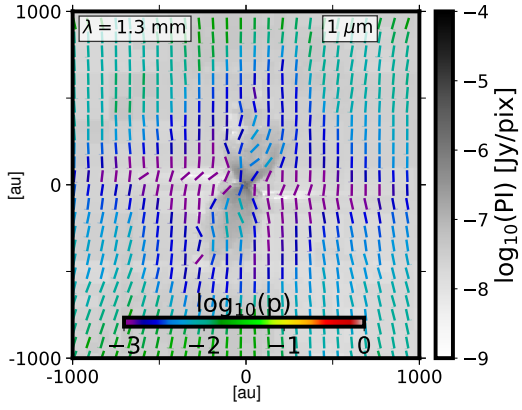


Figure A8. Perfect synthetic observation at $\lambda = 1.3 \text{ mm}$ for the dust population of small grains ($a_{\text{max}} = 1 \mu\text{m}$) composed of only astrosilicates. This figure shows that, not even for this favored dust composition, dust size distributions lacking of dust grains bigger than $10 \mu\text{m}$ do not reproduce the expected polarization degree.